Microelectronic Engineering 288 (2024) 112143

Contents lists available at ScienceDirect

Microelectronic Engineering

journal homepage: www.elsevier.com/locate/mee

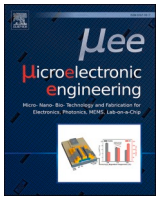

Laser induced reverse transfer of bulk Cu with a fs-pulsed UV laser for microelectronics applications

Tommaso Raveglia, Dario Crimella, Ali Gökhan Demir *

Department of Mechanical Engineering, Politecnico di Milano, Via La Masa 1, 20156 Milan, Italy

ARTICLE INFO

Keywords:
Laser induced backward transfer
LIRT
LIBT
Copper
Femtosecond laser
Single-step deposition
Additive manufacturing

ABSTRACT

Laser Induced Reverse Transfer (LIRT) is a versatile technique as a single-step deposition method allowing the localized transfer of a variety of different metals and polymers on transparent, ultra-thin and stretchable substrates. Also referred to as laser induced backward transfer (LIBT), the process can be manipulated to transfer material from bulk materials to transparent targets, providing a direct method potentially sustainable to generate microelectronic circuitry. In this work, a fs-pulsed UV laser (343 nm) was employed for the first time to transfer electrically conductive copper tracks and layers from bulk Cu in the form of sheet metal onto ultra-clear soda lime glass slides with sub-micrometric thickness. The process development started from the selection of the materials for adequate energy transfer between the beam source and the donor/receiver combination. In the single-track study, the effect of donor/receiver gap was analyzed while tracks ranges with 5 to 233 nm thickness and 7 to 41 μm average width were produced. Based on the results, multi-track layer deposition was assessed by varying the overlap between the tracks. Functional demonstrator cases were produced. The work confirms the suitability of LIRT as a direct approach to create microelectric circuitry by using readily available and sustainable bulk Cu material.

1. Introduction

Material ablation assisted by short and ultrashort pulsed lasers gained an increasingly important role in microfabrication and deposition of thin films over the last three decades. Due to the ultrashort light-matter interaction, fs-pulsed lasers cause negligible thermal damage to the target material, becoming one of the most interesting tools for material processing in the micro scale. Laser fluence over a certain threshold value causes material evaporation, with ejection of nanometric sized particles, or photo-dissociation, depending on the target nature. Material ejection and transfer due to laser ablation can be exploited as a single step-patterning technique, based on the application, for etching or deposition purposes. Single-step deposition based on laser ablation might be a cheaper, faster, and sustainable alternative for the production of microelectronic devices, substituting conventional complex multi-step processes. Some of the first results on laser induced forward transfer (LIFT), a very interesting variation of laser ablation and deposition, were reported by Bohandy et al. in 1986 [1]. They deposited Cu lines of 60 μm at 139 mJ pulse energy and 40 μm lines at 110 mJ of pulse energy using high energy excimer laser (193 nm) from a donor on a Si substrate. Unlike laser ablation, which was mainly used for thin film deposition on large areas, laser-induced transfer is suitable for deposition in specific sites of the substrates of small droplets, tracks, or complex patterns with spatial resolution in the micrometric scale. LIFT was first introduced as a direct microprinting technique based on laser ablation, but the need of a thin film source involves several complex procedures [2]. Laser Induced Reverse Transfer (LIRT) is the counterpart of this mechanism, and the differences are related to the characteristics of the donor and the receiver substrates. The process is also often referred to as Laser Induced Backward Transfer (LIBT), where a pulsed laser is transmitted through a transparent receiver and focused onto the top surface of a flat target placed in proximity as shown in Fig. 1. Laser radiation is absorbed by the target material, and a small portion of the volume is ablated and transferred to acceptor transparent receiver. Thus, donor material can be either bulk or prepared into a thin film. Even though the need of a transparent receiver might limit its application, LIRT shows intrinsic advantages related to the transfer mechanism from readily available solid samples. In fact, there is no need for specific preparation of the donor substrate, limiting the preliminary steps to the polishing of its surface. LIRT becomes in this way a single step patterning

* Corresponding author.
E-mail address: aligokhan.demir@polimi.it (A.G. Demir).

https://doi.org/10.1016/j.mee.2024.112143
Received 3 August 2023; Received in revised form 23 January 2024; Accepted 23 January 2024
Available online 28 January 2024

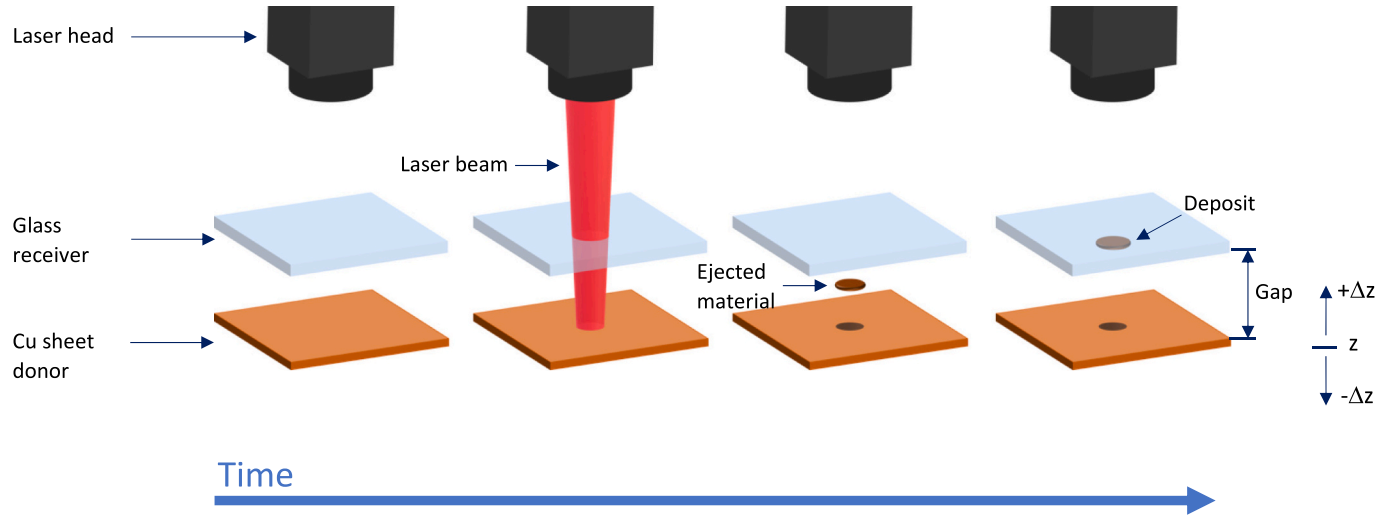

Fig. 1. Functioning principle of laser induced reverse transfer (LIRT) with a solid donor.

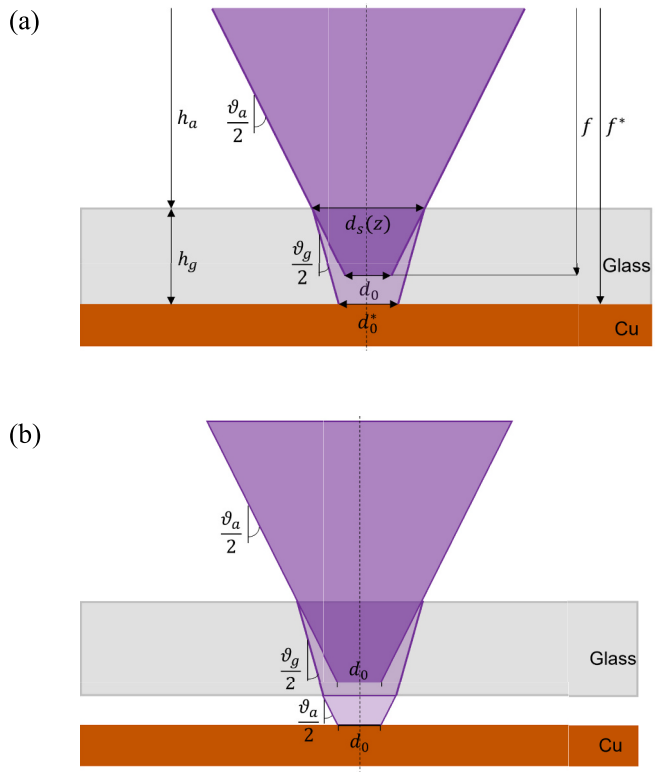

Fig. 2. Schematic representation of the beam propagation in glass reaching the Cu donor without a gap (a). Beam propagation in the presence of a gap (b). The beam propagation is in the vertical direction.

technique, opening the field to the transfer of several materials whose preparation into thin film was too challenging or expensive, thus unsuitable for the LIFT process. LIRT applications are countless, mostly in the fields of fabrication of sub-micrometric structures [3,4], microelectronics [5,6], optics and bioengineering [7]. In literature, LIRT has been used for dry printing of small conductive circuits and electrodes [5,6,8], fabrication of diffractive structures [3,9–11], fabrication of monochromatic reflectors on stretchable substrates [12], deposition of Au nanodroplets [12,13] and thin structures [4,14,15], deposition of Bi_2O_3 films [16]. The technique suits to transfer a variety of materials, including metals such as gold, copper [11,17–19], silver [8,20,21], aluminium [5,21,22], but also polymers [23–25] and C based materials [26,27]. The LIRT process has been studied on several materials with large area applications moving towards the industry [28]. Concerning the increased commercial availability of the high-power ultrashort pulsed laser sources the use of LIRT process may be expanded towards a more flexible usage with materials available in sheet metal form also reducing the deposited layer dimension to nanometric range. However, systematic works showing the process development putting together the material choice, the system design, and parameter study appear to be missing in the literature.

Large-area electronics has put forward laser-induced transfer processing for producing conductive patterns from liquid-deposited and pastes [29]. All these processes exploit the preparation of dedicated materials engineered to the final application requirements but also for the deposition possibility by the dedicated process. The technique suggested in this paper is based on solid metals in the sheet form. The direct availability of the material renders the approach economically appealing and environmentally sustainable. Moreover, in the last decade, the ultrashort pulsed solid-state lasers have become more productive and reliable, fitting into smaller footprints, and requiring much less stringent manufacturing environments. Along with a reduction of capital and usage costs, their industrial presence expanded through material removal-based micromachining applications. In the meanwhile, the need for sustainable and environmentally benign processes grows also for the most challenging and established sectors as microelectronics. The use of bulk materials, such as sheet metal, and direct writing techniques employed in ambient atmosphere can be further exploited from such perspective. Indeed, the process capabilities in terms of geometric resolution and surface quality should be better evaluated.

In the present work, Cu was deposited by LIRT using UV fs-pulsed laser onto ultra-clear soda lime glass often employed in displays and consumer electronics. Cu tracks and layers were direct deposited from sheet metal at ambient atmosphere, making the approach simple and sustainable, without the need for preliminary steps. The first part of the research concerns the study of the laser beam propagation between donor and receiver in order to choose materials and proceed to the system development. In the second part, the effect of process parameters, such as scan speed, laser fluence and pulse repetition rate, on the width and thickness of the deposited features is investigated in detail with specific experimental campaigns. The effect of the air gap thickness between donor and receiver is also analyzed. In the last part, the potentials of LIRT technology are highlighted through the direct printing of complex patterns characterized by sub-micrometric features.

2. Modelling of laser beam propagation between donor and receiver

In LIRT, the laser beam passes through a transparent receiver medium. During this passage the beam divergence changes, thus the focal length and the spot diameter change. The addition of a glass receiver introduces interfaces for reflection between air and glass and between glass and the target material. The light transmitted through the receiver will be also attenuated, as a function of the glass height. In the following, the effect of refraction due to the passage between different media (air-glass) has been modelled neglecting possible diffraction effects in the limited thickness of the glass receiver (in the order of 1 mm). The propagation of beam inside the glass substrate is schematized in Fig. 2a. In this case the beam propagation changes, and the beam interacts with the Cu donor at a newly developed glass-Cu interface. In the case when a gap of air is present downstream of the glass substrate, as seen in Fig. 2b, the second interface glass-air refracts again the laser beam, thus changing again the divergence angle to the value calculated upstream of the glass. In this case, the presence of the glass receiver imposes a change of the focal position only, which can be directly adjusted. Accordingly, the condition with no gap requires further modelling to assess the change in the energy transfer (Fig. 2a). The nominal peak fluence for a Gaussian beam shape can be calculated as,

$$F_0 = \frac{8E}{\pi d_0^2} \tag{1}$$

where E is the energy emitted by the laser and d_0 is the spot diameter at the nominal focal position calculated at $1/e^2$ of the peak fluence. Passing through the glass receiver the beam energy is attenuated: E_t is the transmitted energy reaching the workpiece and the beam size is enlarged to d_0^* on the workpiece. Both transmitted energy and spot diameter depend on the glass thickness. To calculate the transmitted energy on the workpiece, the reflections at the interfaces and the attenuation are considered according to Beer-Lambert as in Eqs. (2) and (3).

$$E_t = \left(1 - R_{ag}\right) E e^{-\alpha h_g} \left(1 - R_{gCu}\right) \tag{2}$$

$$E_t = \left(1 - R_{ag}\right) E e^{-\alpha h_g} \left(1 - R_{ga}\right) \left(1 - R_{aCu}\right) \tag{3}$$

where E is the laser energy, R_{ag}, R_{ga} and R_{gCu} are, respectively, the reflectivity at air-glass, glass-air and glass-solid interfaces, α is the absorption coefficient of glass, and h_g is the transparent receiver thickness. Eq. (3) refers to the case in which a small air gap is present between the transparent receiver and the target material, thus different interfaces for light reflection give different values of transmitted energy. Reflectivity and absorptivity properties of a material define the complex refractive index, as expressed by Eq. (4):

$$\tilde{n} = n + ik \tag{4}$$

where n is the real part of the refractive index and k is the extinction coefficient [30]. The absorption coefficient hence is calculated using extinction coefficient for a given wavelength (λ) using Eq. (5):

$$\alpha = \frac{4\pi k}{\lambda} \tag{5}$$

Instead, the reflectivity at the interface between two media can be calculated with normal incidence approximation because of the low divergence angle of the laser, as shown by Eq. (6).

$$R_{ij} = \left| \frac{\tilde{n}_i - \tilde{n}_j}{\tilde{n}_i + \tilde{n}_j} \right|^2 \tag{6}$$

The subscripts indicate the complex refractive index corresponding to different media. To calculate the beam radius on the workpiece the beam divergence change should be considered. Beam divergence in air (ϑ_a) after the focal lens before reaching the glass can be estimated through Eq. (7).

$$\vartheta_a = \frac{d_c}{f} \tag{7}$$

The beam diameter at the focal point is calculated with the following Eq. (8):

$$d_0 = \frac{4M^2 \lambda f}{\pi d_c} \tag{8}$$

where M^2 is the beam quality factor, λ is the wavelength, f is the focal length, and d_c is the collimated beam diameter. The beam divergence change, due to the passage of light through the interface between two different media, can be calculated according to Snell's law. For the specific case of laser beam passing from air into a glass substrate, the beam divergence lowers, which also implies a variation the geometrical position of the focal point. Thus, the modified focal length f^* is greater than the initial f. The Snell's law can be written as Eq. (9), where ϑ_g is the refraction angle in glass.

$$n_a \sin\frac{\vartheta_a}{2} = n_g \sin\frac{\vartheta_g}{2} \tag{9}$$

Rewriting Eq. (9), the refraction angle in glass can be calculated as shown in Eq. (10):

$$\vartheta_g = 2 \bullet \sin^{-1}\left(\frac{n_a}{n_g}\sin\frac{\vartheta_a}{2}\right) \tag{10}$$

where n_a and n_g are the refractive index of air and glass, respectively. Since the refraction angle ϑ_g is smaller than the divergence angle of the laser beam in air ϑ_a, the geometrical focus position moves farther away from the focusing lens. Therefore, to calculate the new position of minimum spot diameter in presence of the glass substrate d_0^*, the modified focal length f^* caused by the change of the geometrical focus position needs to be defined. As shown in Fig. 2, the modified focal length depends on the distance between the focal lens and the surface of the glass, h_a, and on the glass thickness, h_g. The beam will focus on a new point at the underside of the glass receiver, so the modified focal length will be calculated with Eq. (11).

$$f^* = h_a + h_g \tag{11}$$

In LIRT process, the transparent receiver thickness is usually a constraint, depending on the application. Therefore, h_g is a process parameter, while h_a needs to be calculated. The spot size at a given Δz distance from the focal point can be calculated through the caustic equation as expressed in Eq. (12).

$$d_s^2(z) = d_0^2 + \Delta z^2 \vartheta^2 \tag{12}$$

Considering the two optical paths shown in Fig. 2, the one propagating in air and the one propagating inside the glass, the beam size on the receiver surface can be used as a reference point where d_s is the same for the two optical paths. Eq. (13) describes this equivalence.

$$d_s^2(z) = d_0^2 + \Delta z_a^2 \vartheta_a^2 = d_0^{*2} + \Delta z_g^2 \vartheta_g^2 \tag{13}$$

Δz_a is the distance between glass top surface and the virtual position of d_0 and is equal to $f - h_a$, and Δz_g is equal to h_g. In Eq. (13), the new waist spot diameter in the glass d_0^* can be calculated with the modified focal length f^* through Eq. (14).

$$d_0^* = \frac{4M^2 \lambda f^*}{\pi d_c} = \frac{4M^2 \lambda \left(h_a + h_g\right)}{\pi d_c} \tag{14}$$

In Eq. (13) the unknown terms can be substituted with their definitions to get the following quadratic form (Eq. (15)):

Table 1
Main specifications of the employed laser system.

Parameter	Value
Pulse duration, τ [fs]	214
Collimated beam diameter, d_c [mm]	3.76
Pulse repetition rate, PRR [kHz]	400
Wavelength, λ [nm]	343
Maximum power, P_{max} [W]	3
Maximum pulse energy, E_{max} [μJ]	7.5
Beam quality, M^2 [−]	<1.2
Power distribution	Gaussian
Polarization	Horizontal

Table 2
Optical properties of the donor and the receiver at 343 nm [31].

Property	Receiver	Donor
Material	Ultra-clear soda lime glass	Pure Cu (99.99%)
Thickness, h [mm]	1.05	0.60
Refractive index, n [−]	1.546	1.3702
Extinction coefficient, k [−]	2.235×10^{-6}	1.8705

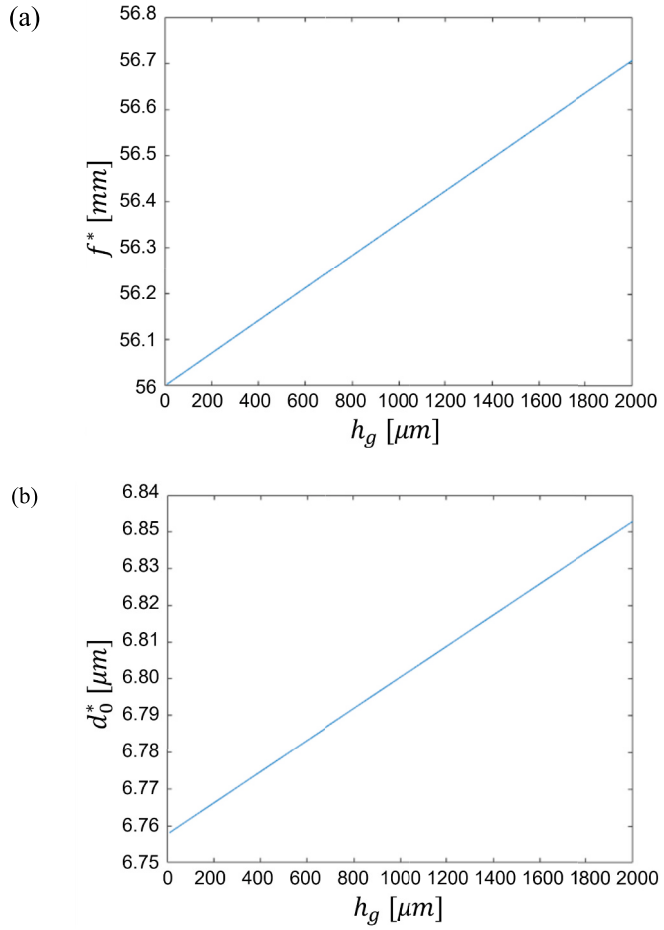

Fig. 3. Change in f and d_0 through ultra-clear glass in the case of no-gap condition. New focal length f* (a), and new waist diameter d_0* (b) as a function of the receiver thickness.

$$\left(C^2-\vartheta_a^2\right)h_a^2+\left(2h_gC^2+2f\vartheta_a^2\right)h_a+\left(C^2+\vartheta_g^2\right)h_g^2-\left(C^2+\vartheta_a^2\right)f^2=0 \tag{15}$$

where C is a constant, expressed by Eq. (16).

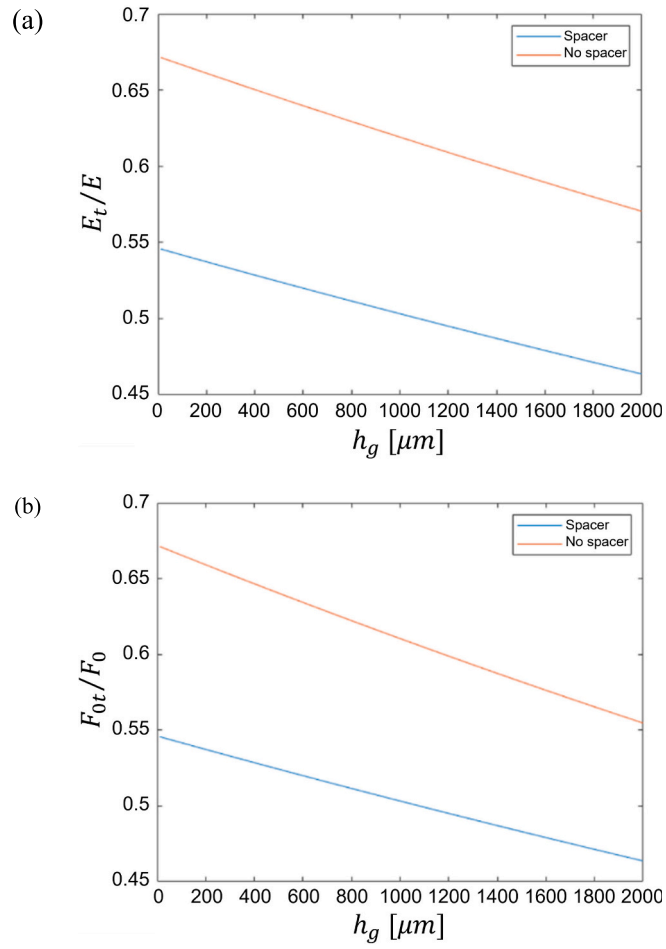

Fig. 4. Light attenuation due to the presence of a transparent receiver. Transmitted energy attenuation (a), and laser fluence attenuation (b).

$$C=\frac{4M^2\lambda}{\pi d_c} \tag{16}$$

Eq. (15) can be solved to obtain h_a as a function of h_g. The second order equation will give two solutions for h_a, but only one solution respects the physical condition of $h_a < f$. Once h_a is calculated, the waist diameter of the laser beam in glass d_0^* and the new focal length f^* can be calculated through Eqs. (11) and (14).

Since during LIRT processes the geometrical focal position inside the glass is positioned on the target material, Eq. (1) can be rewritten implementing Eqs. (2) and (3) to calculate the transmitted fluence interacting with the donor material, obtaining Eqs. (17) and (18).

$$F_{0t}=\frac{8E_t}{\pi\left(d_0\left(h_g\right)\right)^2}=\frac{8}{\pi d_0^{*2}}\left(1-R_{ag}\right)Ee^{-\alpha h_g}\left(1-R_{gCu}\right) \tag{17}$$

$$F_{0t}=\frac{8E_t}{\pi d_0^2}=\frac{8}{\pi d_0^2}\left(1-R_{ag}\right)Ee^{-\alpha h_g}\left(1-R_{ga}\right)\left(1-R_{aCu}\right) \tag{18}$$

Eq. (18) refers once again to the case in which a small air gap is present between the glass and the target material. In this case, after the beam passes through the glass, the divergence angle comes back to the previous value ϑ_a, thus the spot diameter in the new focal position is equal to d_0.

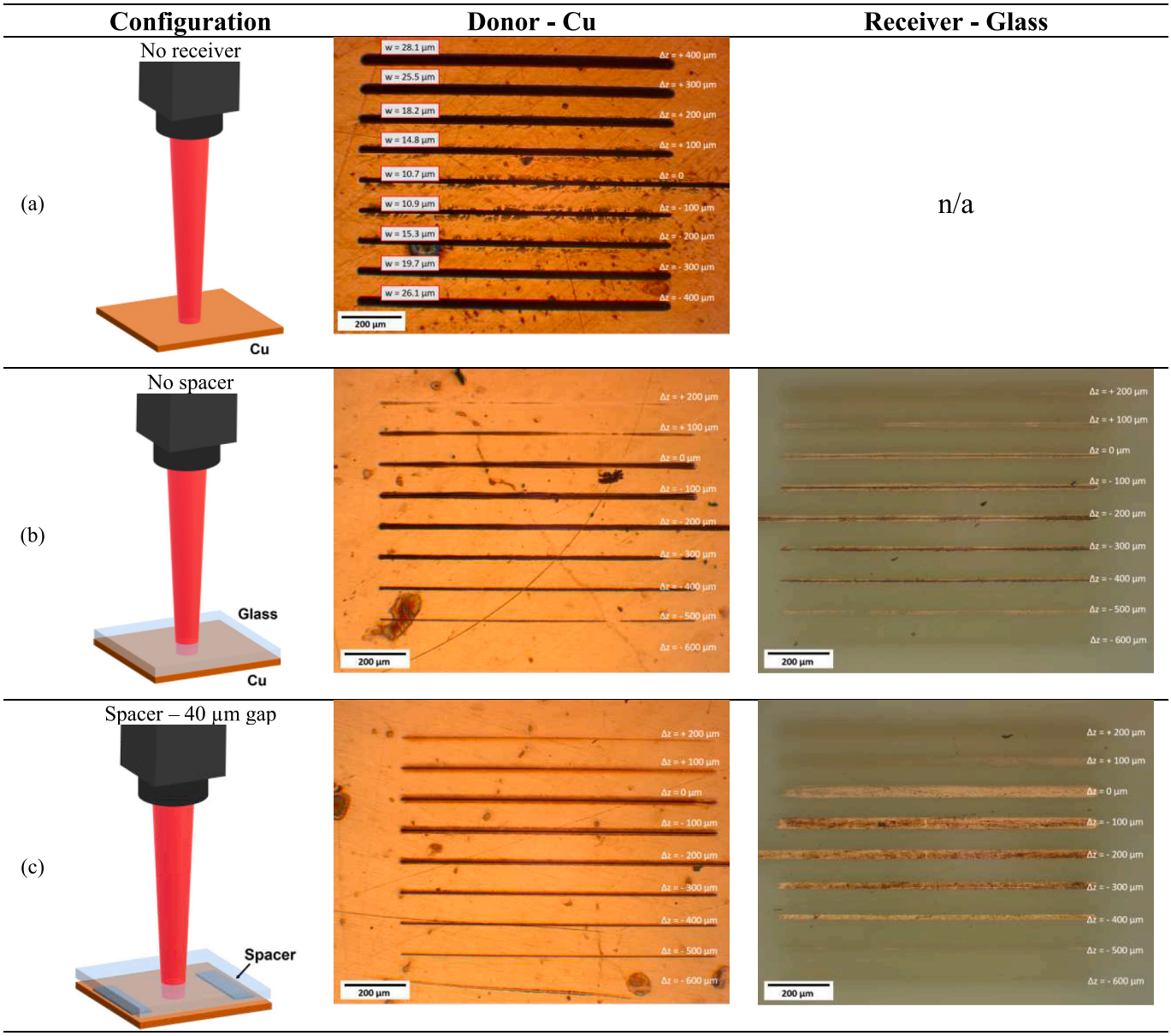

Fig. 5. Schematical representation and light-microscope images of donor and receiver substrate posterior to LIRT processing for the following configurations: (a) no receiver used, (b) no spacer used, and (c) spacer of 40 µm used.

3. Development of the laser induced reverse transfer (LIRT) system

3.1. LIRT system design

The system is based on a solid-state femtosecond laser source (Light Conversion Pharos, Vilnius, Lithuania) which employs direct diode-pumped Yb:KGW as an active medium, and a chirped pulse amplifier, providing average power up to 3 W at UV wavelength (343 nm) with a pulse width of 214 fs. Being the output pulse repetition rate (PRR) of the regenerative amplifier equal to 400 kHz, the laser source is equipped with a pulse picker module which allows to pick the pulses with a desired frequency. Additionally, an internal attenuator is used to regulate the output power of the laser. The laser beam is launched to a scanner head with a 50 mm telecentric focal lens. The beam diameter in the focal position was calculated to be equal to 6.8 µm. Table 1 reports the main specifications of the employed laser system.

Downstream of the optical chain, a 3-axis moving stages with a 0.1 µm precision is installed (Aerotech, Pittsburgh, PA, USA), thus allowing the precise movement of the workpiece under the laser head, together with the control on the focal position.

Optical microscopy was used throughout the work for qualitative assessment of the process on the donor and the receiver sides (UM300I, EchoLAB, Paderno Dugano, Italy). Confocal microscopy was used to acquire 3D reconstruction of the deposits with 1 nm axial resolution (MahrSurf CWM 3000, Mahr, Göttingen, Germany). SEM images were taken, and chemical composition analysis was executed through EDS (EVO 50, Zeiss, Oberkochen, Germany).

3.2. Donor and receiver materials

Pure copper (99.99% purity) sheets with 0.6 mm thickness were used as donor material. As a principal material used in electronics, Cu was chosen for its availability to be employed in a wide range of applications. Samples were cut in 27 mm × 27 mm squares, polished to homogenize the surface, and finally cleaned with isopropyl prior to the experiments.

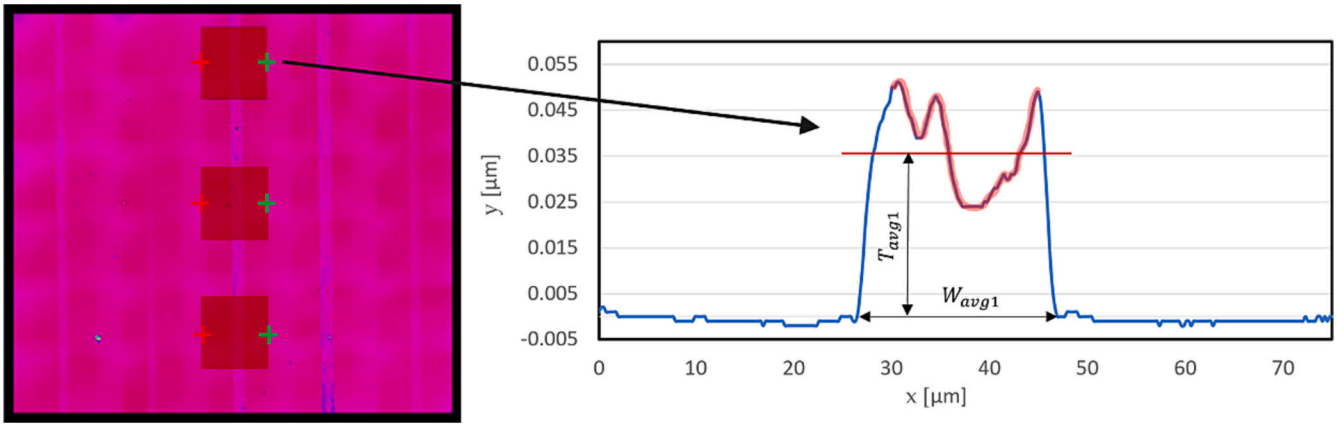

Fig. 6. Measurement procedure for $\mathbf{T_{avg}}$ and $\mathbf{W_{avg}}$. The left panel shows the acquired deposition lines and the traced measurement zones, where each measurement is traced between a red and a green cross. The right panel shows the height profile of the traced line. (For interpretation of the references to colour in this figure legend, the reader is referred to the web version of this article.)

Table 3
Process parameters for LIRT without a spacer.

Fixed parameters	
Gap between donor and receiver, h_s [µm]	0 (direct contact)
Varied parameters	
Scan speed, v [mm/s]	2, 15, 28, 41
Pulse Repetition Rate, PRR [kHz]	25, 50, 100, 400
Laser fluence, F [J/cm^2]	0.84, 5.18, 9.51, 13.85, 18.18

As received soda-lime glass has been chosen as it is extensively used in different industries including displays and consumer electronics (eg. smartphones, tablets, touch screens). Moreover, it is characterized by high recyclability. The receiver substrate needs to be highly transparent in the UV region, thus ultra-clear soda-lime glass was chosen. The glass was purchased in form of 1.05 mm thick 30 mm × 30 mm square shaped slides (Qingdao Vatti Glass Co, Jiaozhou Qingdao City, China). Table 2 shows the optical properties of the donor/receiver materials.

4. LIRT process development with a fs-pulsed UV laser

4.1. Beam attenuation through the donor/receiver system

With the chosen material configuration, the beam propagation was calculated first for no-gap condition. In Fig. 3(a) and (b) the new focal length f^* and the new waist diameter d_0^* are plotted as a function of the glass thickness. According to the modelled beam propagation, in the absence of gap the focal point was shifted approximately by 370 µm below the nominal position, increasing the effective focal length. On the other hand, the increase of the waist diameter is in the order of 0.7%, thus it can be neglected.

The energy transmittance and the fluence change on the workpiece

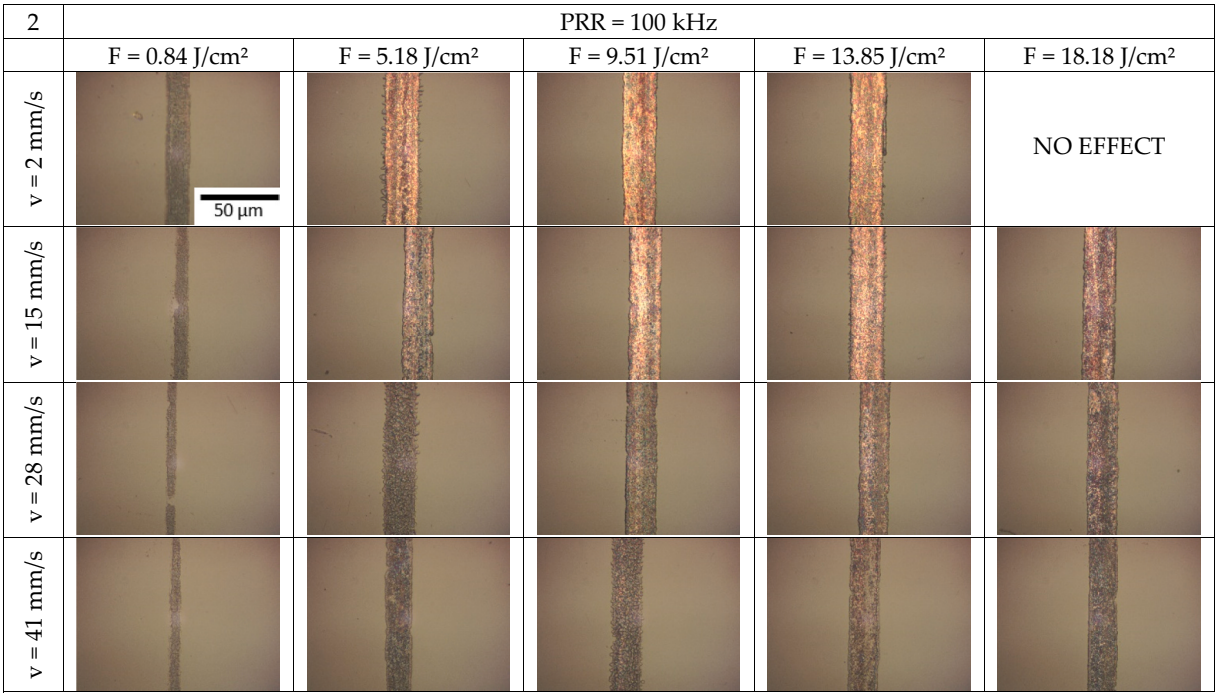

Fig. 7. Light-microscope images of receiver substrate after LIRT processing without a spacer using pulse repetition rate (PRR) at 100 kHz and varying the scan speed (v) and the fluence (F).

was calculated for two conditions namely i) no spacer, where no gap was employed, and ii) spacer, where a 40 μm gap condition also used in the experiments was considered. Fig. 4 shows the transmittance expressed as the proportion of transmitted energy to incident energy on the glass surface as a function of glass thickness. A large fraction of energy is lost due to reflections at the interfaces and the difference between the transmitted energy in the two cases with and without the spacer is due to the different interfaces for reflection.

To validate the modelled behavior, simple marking experiments were carried. Three conditions namely i) no receiver, ii) no spacer, iii) spacer – 40 μm gap were assessed as shown in Fig. 5. Linear incisions were made with $F_0 = 9.51$ J/cm^2 nominal peak fluence at 100 kHz pulse repetition rate and 2 mm/s scan speed. The position of the Cu donor surface was varied along the beam propagation direction (Δz) with 100 μm step. Cu and glass surfaces were observed qualitatively with the optical microscope with the aim of evaluating the actual focal position change.

As seen in Fig. 5, the thinnest marking in the case of no receiver corresponds to the nominal focal position (Δz = 0). In the case of "no spacer", at Δz = 0, the incision is unstable and the material transfer to the receiver is limited. Instead at Δz = −300 μm, the incisions on the donor side are thin and material is correctly transferred to the receiver end, which is coherent to the model. In the "spacer – 40 μm" condition a similar focal position shift is observed. At the nominal focal position (Δz = 0), the incision is wider, while at Δz = −200 μm both the incision on the donor and the deposit on the receiver become more stable. The results also confirm that the presence of a spacer allows for a better material transfer avoiding the glass-Cu interface. In the experimental phase, both the conditions without and with the use of spacer were further investigated at their respective focal positions to better understand the effect of the spacer on the deposit morphology.

4.2. Single track deposition

Within the single-track deposition, the main process parameters regulating the energy transfer were studied without and with spacer separately as these conditions determined different processability windows due to different beam attenuation levels. In particular, the nominal peak fluence, pulse repetition rate, and scan speed were studied. All the experiments were executed in a randomized way, and two replicates of each experimental point were tested using two different Cu samples and two different glass slides. After the deposition, the glass surface was cleaned by hand using a cloth for lens cleaning and some alcohol: cleaning helps to remove some metal debris that were ejected towards the receiver but have no adhesion with the glass surface or with the other metal particles.

The geometrical characterization is executed on 3D images captured with confocal microscopy. Based on the obtained scan, it is possible to analyze profiles averaged along the track length, by choosing the number of profiles to be averaged. In this case, 500 profiles were considered, for a length of 124.5 μm. For each single track the average thickness and width are measured on the averaged profiles, three times per track on 3 different regions (top, center, bottom), as shown in Fig. 6. After, the three measures are used to calculate the overall average thickness T_{avg} and average width W_{avg} for each single line according to Eq. (19) and (20).

$$T_{avg} = \frac{T_{avg1} + T_{avg2} + T_{avg3}}{3} \tag{19}$$

$$W_{avg} = \frac{W_{avg1} + W_{avg2} + W_{avg3}}{3} \tag{20}$$

4.2.1. Single track deposition without a spacer

An overview of the combinations of process parameters chosen for this specific set of experiments is shown in Table 3. The nominal fluence

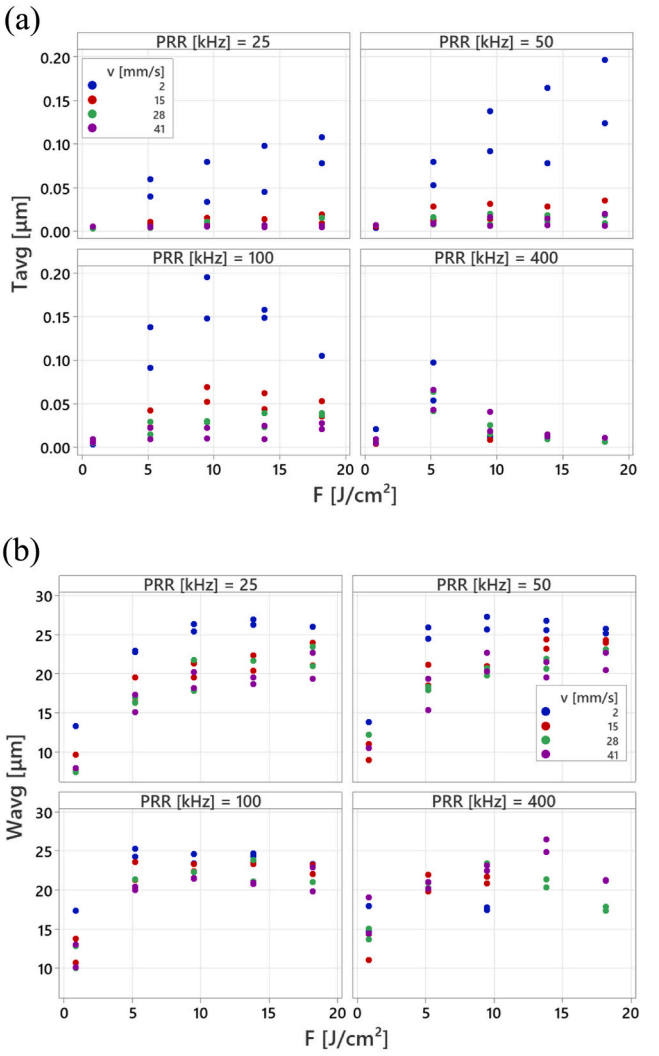

Fig. 8. Effect of pulse repetition rate (PRR), scan speed (v), and fluence (F) on average thickness $\mathbf{T_{avg}}$ (a) and width $\mathbf{W_{avg}}$ (b) of the deposited tracks without a spacer.

was varied between 0.84 and 18.18 J/cm2, while the scan speed was tested between 2 and 41 mm/s, and the pulse repetition was between 25 and 400 kHz.

Fig. 7 shows optical microscopy images of the single tracks obtained without a spacer as a function of scan speed and fluence for 100 kHz pulse repetition rate. Higher fluence and lower scan speeds produce wider and well-defined tracks. On the other hand, at the highest fluence and lowest scan speed, where the highest amount of total energy release is expected, the process appears to produce no deposit. This implies a possible destructive process when energetic conditions are too high.

The effect of the process parameters on the geometrical attributes

Table 4
Process parameters for LIRT with a spacer.

Fixed parameters	
Gap between donor and receiver, h_s [μm]	40
Varied parameters	
Scan speed, v [mm/s]	2, 7, 12
Pulse Repetition Rate, PRR [kHz]	25, 50, 100
Laser fluence, F [J/cm^2]	5.18, 9.51, 13.85, 18.18

can be seen in Fig. 8. For each tested condition two replications were measured, which are plotted together to indicate process variability. The thickness (T_{avg}) increases by increasing fluence and pulse repetition rate and decreases by increasing scan speed. This behavior was expected since a higher amount of energy and a higher overlap between the pulses results in more ablated material, and more deposited material can be expected. It is important to notice the clear change of trend which takes place at 100 kHz increasing the fluence over 10 J/cm^2, where the thickness starts to decrease by increasing the fluence. At 400 kHz the influence of the scan speed is reversed as well as the influence of the laser fluence. In this region, more energy and overlap result in thinner tracks, probably due to removal effect of consecutive pulses.

A similar change of trend at high pulse repetition rate is noticed for the average width (W_{avg}), even though less clearly. Increasing only the laser fluence the track width increases until a certain limit and then starts to slightly decrease, following a trend similar to the one described by Liu's Ablation Model [18]. The average width increases by decreasing the scan speed at 25, 50 and 100 kHz. For the highest levels of fluence at 100 kHz and for all the experiments at 400 kHz the effect of the scan speed in reversed, thus larger width is obtained with faster scan speed. Evidently too high pulse overlap caused principally by very high pulse repetition rates, in the absence of a spacer may cause a destructive effect on the process.

4.2.2. Single track deposition with a spacer

The influence of process parameters on the single tracks with a 40 µm spacer was also assessed. The nominal fluence was varied between 5.18 and 18.18 J/cm^2, while the scan speed was tested between 2 and 7 mm/s, and the pulse repetition was between 25 and 100 kHz. The combinations of process parameters chosen for this specific set of experiments is shown in Table 4.

Fig. 9 shows the optical microscopy images of the single tracks obtained at 100 kHz pulse repetition rate with 40 µm spacer. The results show a similar behavior compared to the no-spacer tests where higher fluence and lower scan speeds produce wider and darker deposits, signs of an increased amount of material transfer. On the other hand, the tracks appear wider overall compared to the no spacer condition.

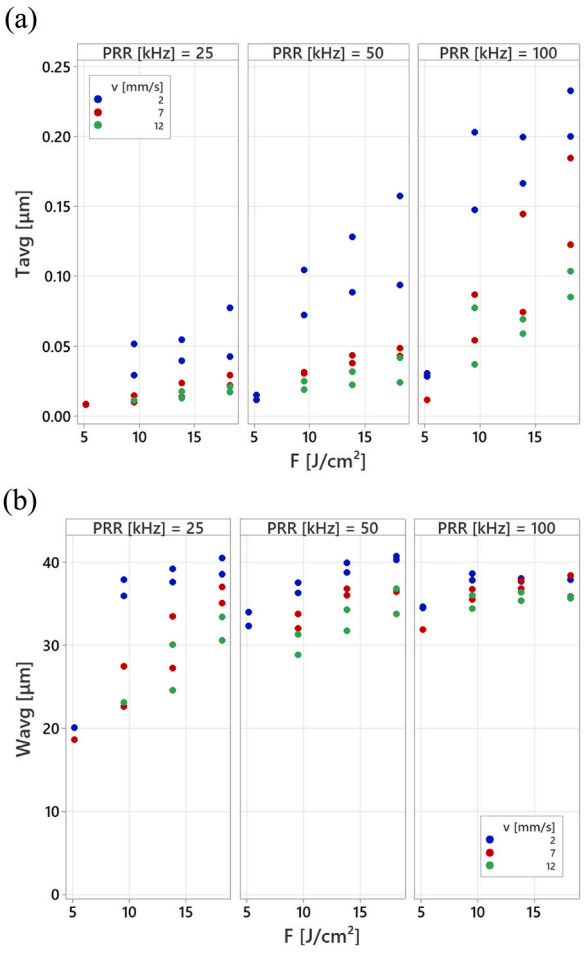

Fig. 10. Effect of pulse repetition rate (PRR), scan speed (v), and fluence (F) on average thickness $\mathbf{T_{avg}}$ (a) and width $\mathbf{W_{avg}}$ (b) of the deposited tracks with 40 µm spacer.

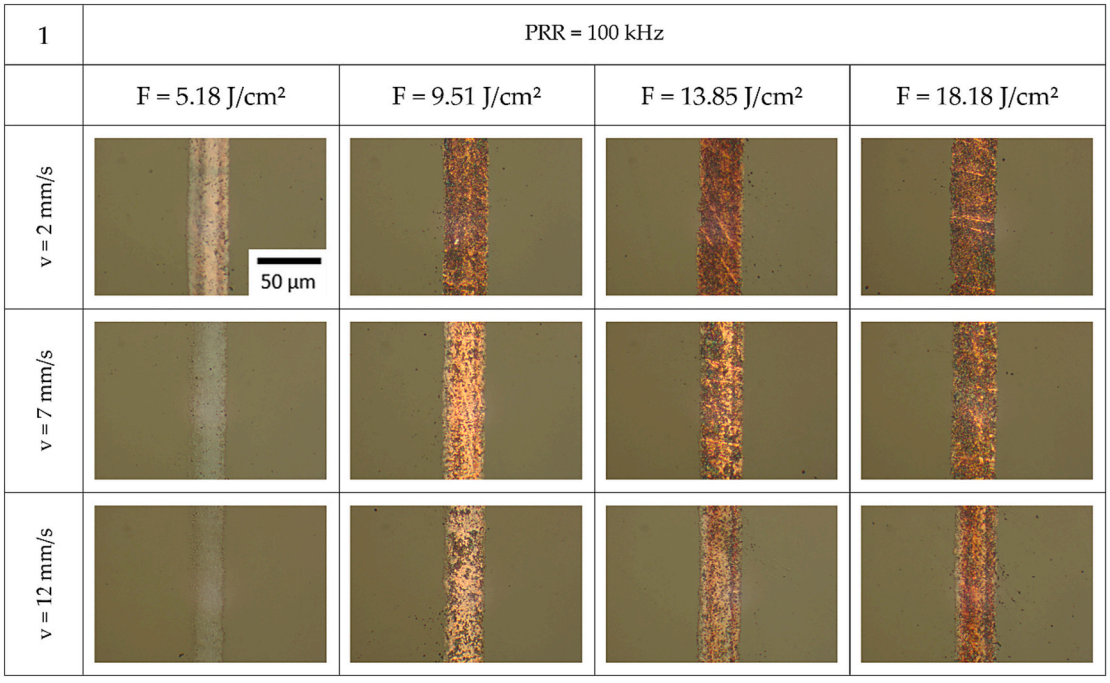

Fig. 9. Light-microscope images of receiver substrate after LIRT processing with a 40 µm spacer using pulse repetition rate (PRR) at 100 kHz and varying the scan speed (v) and the fluence (F).

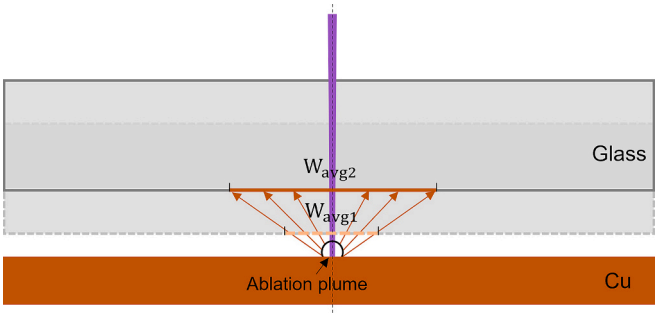

Fig. 11. Schematic representation of the ablation plume expansion in LIRT showing the glass reciever in two separate positions. With a smaller gap a smaller width (W_{avg1}) is expected, whil and increase in the gap should provide a wider track (W_{avg2}) The beam propagates in the vertical direction in the schematic description.

Table 5
Process parameters for the base tracks.

T [μm]	F [J/cm^2]	v [mm/s]	PRR [kHz]
0.09	9.51	2	100
0.18	13.85	2	100
0.22	18.18	2	50

Table 6
Process parameters for multi-track layer deposition by LIRT.

Fixed parameters	
Gap between donor and receiver, h_s [μm]	40
Varied parameters	
Track average thickness, T [μm]	0.09, 0.18, 0.22
Overlap between the tracks, O [%]	0, 12.5, 25, 37.5, 50

The graphs in Fig. 10 show the influence of the process parameters on T_{avg} and W_{avg}. For each tested condition two replications were measured, which are plotted together to indicate process variability. The average thickness increases by increasing fluence and pulse repetition rate and decreases by increasing the scan speed. The average width increases by increasing the laser fluence and by decreasing the scan speed. The pulse repetition rate appears to have a less marked effect on the track in the experimented region. However, concerning the material volume build up higher pulse repetition rate along with the higher fluence and lower speed appear to provide an increase.

Along with the fact that the presence of gap improves the energy transfer to the donor, the difference in terms of the deposition width with the spacer can be attributed the expansion of the ablation plume and shockwave. The ablation plume can be seen as a bubble which enlarges due to the overpressure developed at the metal surface, thus a higher air gap between donor and receiver eases this expansion and the metal particles are spread over a wider area. Thus, the tracks width increases when the spacer thickness increases, and the lowest width is theoretically achieved in the limit case of spacer thickness equal to zero. A schematic representation of this phenomenon is depicted in Fig. 11.

4.3. Multiple-track deposition study

In the light of the single-track deposition study, multiple-track deposits were produced with 40 μm gap between. Square deposits with 0.4 mm × 0.4 mm dimensions were produced. The overlap (O) between each track of the single layers is controlled through the hatch distance (h) as in the following the expression:

$$O = \frac{W_{awg} - h}{W_{avg}} \bullet 100 \tag{21}$$

From the single-track experiments 3 distinct conditions providing different deposit thicknesses were considered to produce thicknesses between 0.09 and 0.22 μm as shown in Table 5. The overlap was varied between 0% to 50%. For each condition the hatch distance was calculated. Table 6 shows an overview of the combinations of process parameters chosen for this specific set of experiments.

Surface characterization was executed considering the entire surface of the deposited layer as depicted in Fig. 12. The average height of the selected area S_a [μm] was measured. In order to assess the deposit homogeneity, the autocorrelation length S_{al} [μm] was measured. The autocorrelation length is defined as the horizontal distance of the auto correlation function which has the fastest decay to the value 0.2. Thus, large values indicate surfaces dominated by low frequencies while small values indicate surfaces dominated by high frequencies.

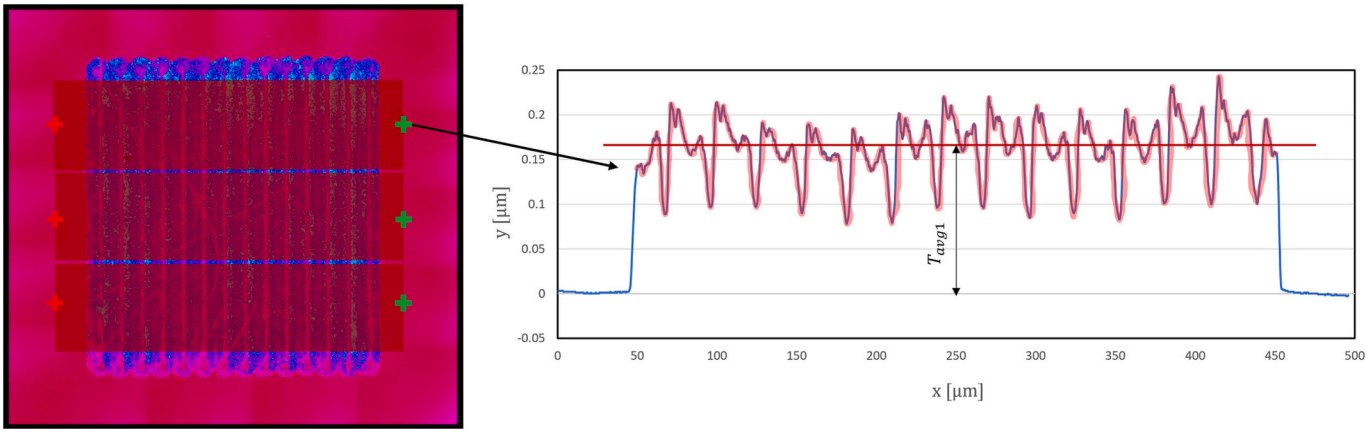

Fig. 12. Measurement procedure for $\mathbf{T_{avg}}$ and surface roughness for multi-track deposition experiments. The left panel shows the acquired deposition lines and the traced measurement zones, where each measurement is traced between a red and a green cross. The right panel shows the height profile of the traced line. (For interpretation of the references to colour in this figure legend, the reader is referred to the web version of this article.)

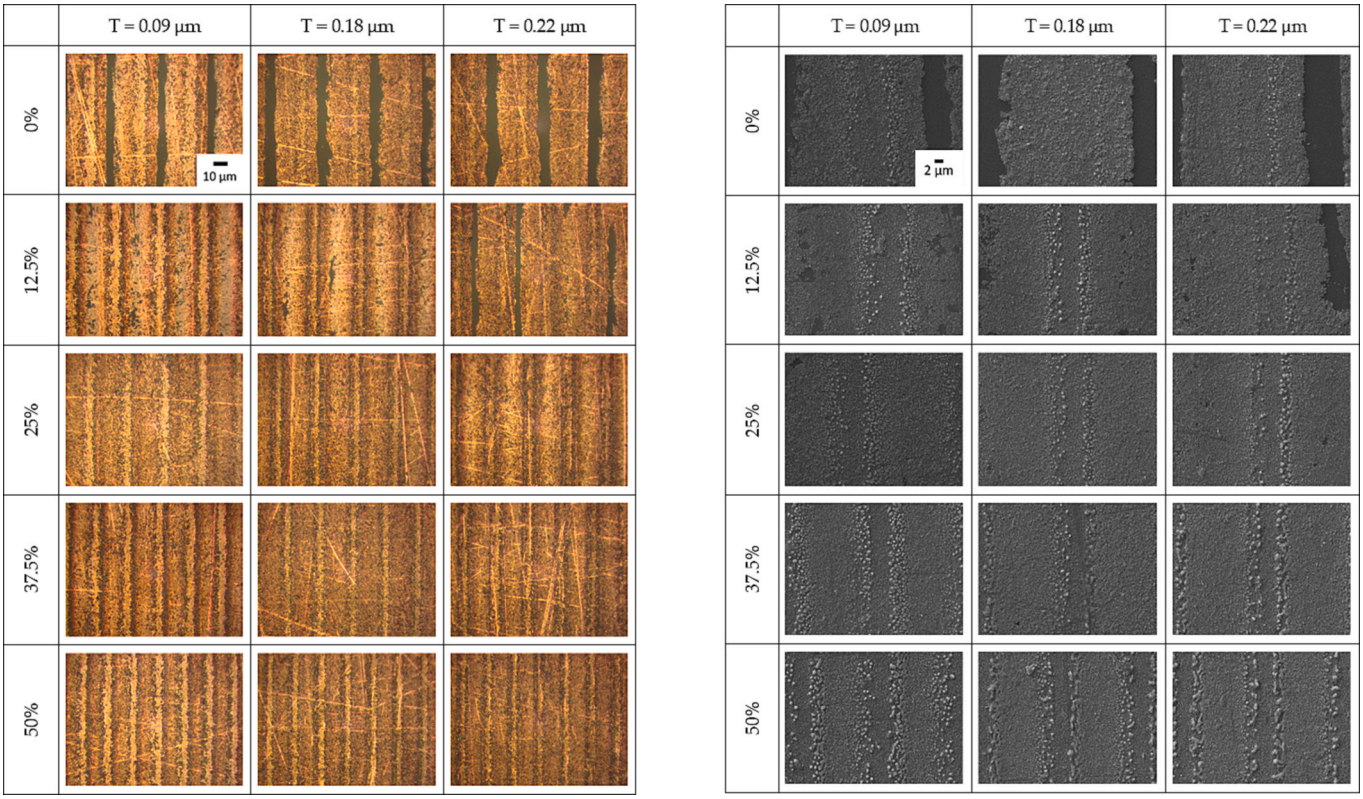

Fig. 13. Optical microscopy and SEM images of the deposited layers as a function of single-track thickness (T) and overlap (O).

4.3.1. Deposit morphology and geometrical attributes

Fig. 13 shows the optical microscopy and SEM images of the samples produced in the multi-track deposition study. It is noted that the deposition is inhomogeneous with overlap 0% and 12.5% as regions with no material deposited are present within the layer. At 0% overlap the tracks are clearly separated by a gap of clean glass, while at 12.5% some holes are visible within the layer and their size increases as the single-track thickness (T) increases, most likely due to the higher fluence involved.

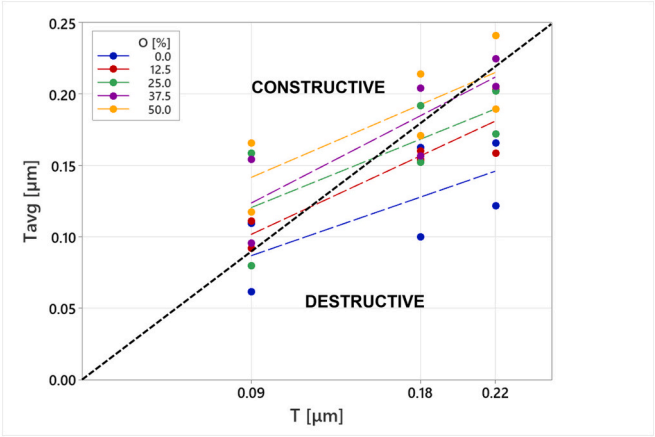

Fig. 14. Effect of single-track thickness (T) and overlap (O) on $\mathbf{T_{avg}}$ of the deposited layers.

Fig. 14 plots thickness T_{avg} of the deposited layer against the thickness of the single track (T). It can be seen that T_{avg} increases as the average thickness of the base line T increases. The same effect is induced by the increase of the overlap (O), most likely due to the superposition of consecutive tracks that progressively increases as O increases. In addition, it is worth noting that T_{avg} can be both higher and lower than the average thickness of the single-track T. Hence Fig. 14 is divided in two regions, defined by "constructive" or "destructive" behavior. While the "constructive" region was expected, due to the overlapping of consecutive tracks, the presence of a "destructive" region in correspondence of higher fluence levels could be explained by a partial removal effect of consecutive tracks on the previously deposited material.

4.3.2. Deposit surface quality

Fig. 15 collects the surface roughness measurements along with a schematic representation of the impact of overlap in the multi-track deposition. Also considering the large variability of the measurements, a minimum for S_a can be detected at 25% employing low and medium T values as seen in Fig. 15a. On the other hand, as seen in Fig. 15b, S_{al} decreases as the overlap increases because more lines are deposited with a shorter hatch distance, thus the surface is progressively dominated by higher frequencies. With a higher level of T the lower frequencies are more accentuated as seen with higher values of S_{al}.

The observed trends can be explained with the help of the schematic representation in Fig. 15c. Starting from 0% overlap, the gaps between the tracks can be filled by increasing the overlap until a certain optimal point, after which the superposition between the tracks results in high peaks and a lower surface quality. Such conditions imply a local minimum at moderate overlap and single layer thickness values.

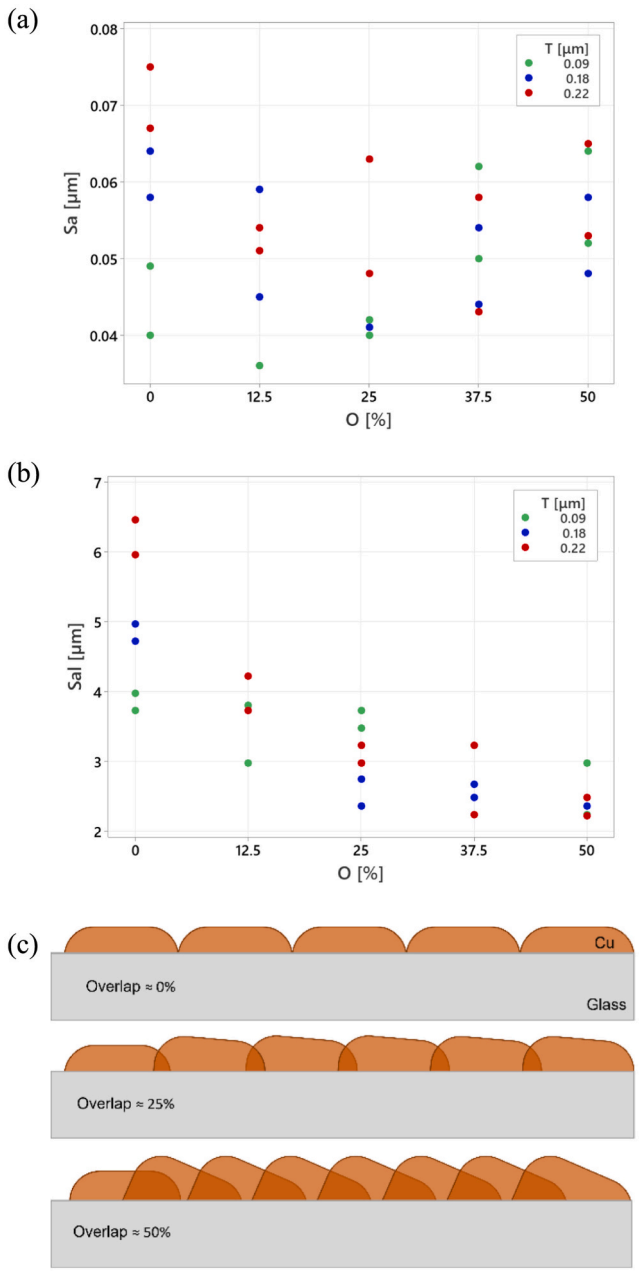

Fig. 15. Effect of the process parameters on S_a (a) and S_{al} (b). Schematic representation of the theoretical influence of O on the surface quality (c).

Cu deposits with simple and complex geometries were produced as demonstrator on glass as seen in Fig. 16. In Fig. 16a a simple circuit is shown, where its electrical conductivity was confirmed via a conventional digital tester. Functional testing of the deposition adherence was not conducted on the produced samples. However, the deposited material was subjected to manual scratching during the electrical conductivity testing using the metallic probe of the digital tester. The scratching did not result in any qualitative difference or any reduction of the electrical conductivity. In Fig. 16c and d the Politecnico di Milano logo is shown in larger and smaller formats highlighting the deposition resolution.

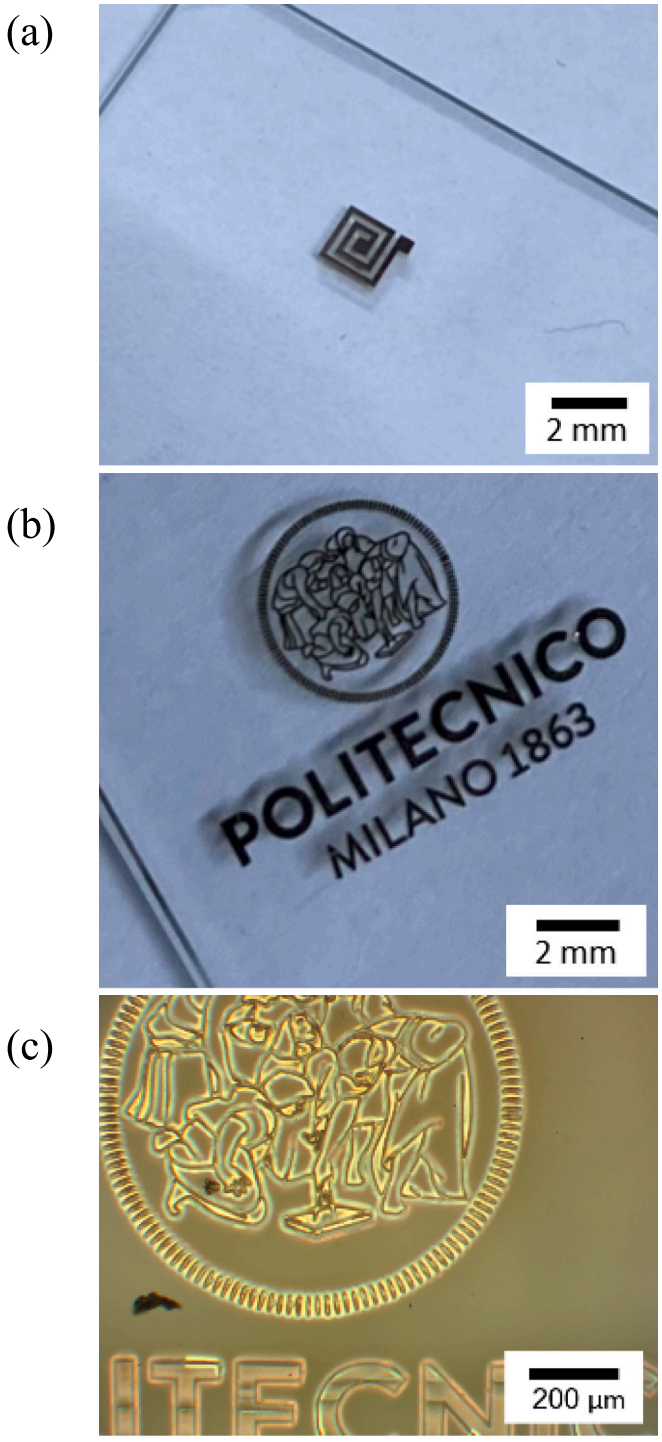

Fig. 16. Examples Cu deposits of glass produced by LIRT. A simple electrical circuit design (a). The institutional logo in large (b) and small (c) size. Process parameters were F = 13.85 J/cm^2, PRR = 100 kHz, h_s = 40 µm, v = 2 mm/s, O = 25%.

5. Conclusions

In the present work, laser induced reverse transfer of pure copper on ultra-clear soda lime glass was analyzed systematically from system design to functional characterization. The effects of different process parameters, such as laser fluence, pulse repetition rate, scan speed and distance between donor and receiver substrates was studied, allowing to achieve a better understanding and control of the process. The work confirms that the contemporary high power ultrafast laser sources combined with bulk metals can constitute a flexible solution for direct deposition of conductive tracks. The process allowed to deposit sub-micrometric layer thicknesses over relatively wide areas up to cm-sizes with a relatively simple arrangement operating at ambient atmosphere. The work confirms that the conceptualized use of commercially available donor materials in sheet metal form can be suitably used for the process. Both the used metal and glass materials are highly recyclable, providing overall a highly sustainable solution. While the work shows the use of a pure metal, LIRT can be expanded to other materials such polymers and ceramic materials separately and in combination. The process can potentially lend itself to one-of-a-kind products and localized deposition options as well as roll-to-roll processing with sub-micrometric deposition. Indeed, the productivity is an aspect that requires further attention. On the other hand, beam shaping solutions for parallel processing can be explored as well as large area processing with dedicated beam shapes.

CRediT authorship contribution statement

Tommaso Raveglia: Conceptualization, Formal analysis, Investigation, Data curation, Software, Writing – original draft, Writing – review & editing. **Dario Crimella:** Conceptualization, Formal analysis, Investigation, Writing – original draft, Writing – review & editing. **Ali Gökhan Demir:** Conceptualization, Methodology, Supervision, Formal analysis, Resources, Investigation, Writing – original draft, Writing – review & editing.

Declaration of competing interest

The authors declare that they have no known competing financial interests or personal relationships that could have appeared to influence the work reported in this paper.

Data availability

Data will be made available on request.

Acknowledgements

This project was supported by Technoprobe S.p.A. The authors are grateful to the technical support of Dr. Christian Piovera, Matteo Borzoni, and Alberto Colombo.

References

[1] J. Bohandy, B.F. Kim, F.J. Adrian, Metal deposition from a supported metal film using an excimer laser, J. Appl. Phys. 60 (4) (1986), https://doi.org/10.1063/1.337287.
[2] P. Serra, A. Piqué, Laser-induced forward transfer: fundamentals and applications, Adv. Mater. Technol. 4 (1) (2019), https://doi.org/10.1002/admt.201800099.
[3] P. Papakonstantinou, N.A. Vainos, C. Fotakis, Microfabrication by UV femtosecond laser ablation of Pt, Cr and indium oxide thin films, Appl. Surf. Sci. 151 (3) (1999), https://doi.org/10.1016/S0169-4332(99)00299-8.
[4] G. Dhami, B. Tan, K. Venketakrishnan, Laser induced reverse transfer of gold thin film using femtosecond laser, Opt. Lasers Eng. 49 (7) (2011), https://doi.org/10.1016/j.optlaseng.2011.02.019.
[5] C.F. Ding, L. Li, H.T. Young, Laser-induced backward transfer of conducting aluminum doped zinc oxide to glass for single-step rapid patterning, J. Mater. Process. Technol. 275 (2020), https://doi.org/10.1016/j.jmatprotec.2019.116357.
[6] J. Macdonald, H. de Fossard, N. Gabbani, W. O'Neill, R. Daly, Material ejection dynamics in direct-writing of low resistivity tracks by laser-induced reverse transfer, Appl. Surf. Sci. 536 (2021), https://doi.org/10.1016/j.apsusc.2020.147924.
[7] N. Safaie, A. Kiani, Enhancement of bioactivity of glass by deposition of nanofibrous Ti using high intensity laser induced reverse transfer method, Vacuum 157 (2018), https://doi.org/10.1016/j.vacuum.2018.08.035.
[8] R. Molina, et al., Laser-induced scanning transfer deposition of silver electrodes on glass surfaces: a green and scalable technology, Appl. Surf. Sci. 556 (2021), https://doi.org/10.1016/j.apsusc.2021.149673.
[9] M.T. Flores-Arias, A. Castelo, C. Gomez-Reino, G.F. de la Fuente, Phase diffractive optical gratings on glass substrates by laser ablation, Opt. Commun. 282 (6) (2009), https://doi.org/10.1016/j.optcom.2008.11.067.
[10] M. Flury, C. Pédri, Laser induced reverse transfer with metal and hybrid material prepared with sol-gel process used on glass substrate, Appl. Surf. Sci. 278 (2013), https://doi.org/10.1016/j.apsusc.2012.11.071.
[11] A. Castelo, et al., Laser backwriting process on glass via ablation of metal targets, Opt. Commun. 273 (1) (2007), https://doi.org/10.1016/j.optcom.2006.12.005.
[12] F. Zacharatos, et al., Laser printing of Au nanoparticles with sub-micron resolution for the fabrication of monochromatic reflectors on stretchable substrates, Opt. Laser Technol. 135 (2021), https://doi.org/10.1016/j.optlastec.2020.106660.
[13] A.I. Kuznetsov, J. Koch, B.N. Chichkov, Laser-induced backward transfer of gold nanodroplets, Opt. Express 17 (21) (2009), https://doi.org/10.1364/oe.17.018820.
[14] A. Logotheti, F. Zacharatos, M. Makrygianni, I. Zergioti, Laser induced backward transfer of ultra-thin metal structures, Appl. Surf. Sci. 512 (2020), https://doi.org/10.1016/j.apsusc.2020.145730.
[15] R. McCann, C. Hughes, K. Bagga, A. Stalcup, M. Vázquez, D. Brabazon, Pulsed laser deposition of plasmonic nanostructured gold on flexible transparent polymers at atmospheric pressure, J. Phys. D. Appl. Phys. 50 (24) (2017), https://doi.org/10.1088/1361-6463/aa7193.
[16] H. Sakata, S. Chakraborty, M. Wakaki, Patterning of Bi2O3 films using laser-induced forward and backward transfer techniques, Microelectron. Eng. 96 (Aug. 2012) 56–60, https://doi.org/10.1016/j.mee.2012.02.002.
[17] Y. Hanada, et al., Development of practical system for laser-induced plasma-assisted ablation (LIPAA) for micromachining of glass materials, Appl. Phys. A Mater. Sci. Process. 79 (4–6) (2004), https://doi.org/10.1007/s00339-004-2614-1.
[18] X. Lu, et al., Laser-induced-plasma-assisted ablation and metallization on C-plane single crystal sapphire (C-Al2O3), Micromachines (Basel) 8 (10) (2017), https://doi.org/10.3390/mi8100300.
[19] Y. Hanada, K. Sugioka, I. Miyamoto, K. Midorikawa, Colour marking of transparent materials by laser-induced plasma-assisted ablation (LIPAA), J. Phys. Conf. Ser. 59 (1) (2007), https://doi.org/10.1088/1742-6596/59/1/145.
[20] F. Rey-García, et al., Microstructure of planar glass substrates modified by laser ablation backwriting (LAB) of metal targets, Appl. Surf. Sci. 307 (2014), https://doi.org/10.1016/j.apsusc.2014.04.091.
[21] W. Zhou, et al., Laser-direct writing of silver metal electrodes on transparent flexible substrates with high-bonding strength, ACS Appl. Mater. Interfaces 8 (37) (2016), https://doi.org/10.1021/acsami.6b07696.
[22] A. Tavangar, B. Tan, K. Venkatakrishnan, Deposition of fibrous nanostructure by ultrafast laser ablation, J. Micromech. Microeng. 20 (5) (2010), https://doi.org/10.1088/0960-1317/20/5/055002.
[23] M. Feinaeugle, D.J. Heath, B. Mills, J.A. Grant-Jacob, G.Z. Mashanovich, R. W. Eason, Laser-induced backward transfer of nanoimprinted polymer elements, Appl. Phys. A Mater. Sci. Process. 122 (4) (2016), https://doi.org/10.1007/s00339-016-9953-6.
[24] M. Feinaeugle, P. Gregorčič, D.J. Heath, B. Mills, R.W. Eason, Time-resolved imaging of flyer dynamics for femtosecond laser-induced backward transfer of solid polymer thin films, Appl. Surf. Sci. 396 (2017), https://doi.org/10.1016/j.apsusc.2016.11.120.
[25] K. Lou, et al., Self-adaptive surface with tunable superamphiphobicity fabricated by femtosecond laser induced backward transfer, Adv. Mater. Interfaces 9 (11) (2022), https://doi.org/10.1002/admi.202102347.
[26] M. Praeger, et al., Laser-induced backward transfer of monolayer graphene, Appl. Surf. Sci. 533 (2020), https://doi.org/10.1016/j.apsusc.2020.147488.
[27] M. Cutroneo, et al., Pulsed laser deposition and laser-induced backward transfer to modify polydimethylsiloxane, Coatings 11 (12) (2021), https://doi.org/10.3390/coatings11121521.
[28] T. Blaudeck, P.A. Ersman, M. Sandberg, S. Heinz, A. Laiho, J. Liu, I. Engquist, M. Berggren, R.R. Baumann, Simplified large-area manufacturing of organic electrochemical transistors combining printing and a self-aligning laser ablation step, Adv. Funct. Mater. 22 (14) (2012) 2939–2948, https://doi.org/10.1002/adfm.201102827.
[29] J. Bian, L. Zhou, X. Wan, C. Zhu, B. Yang, Y.A. Huang, Laser transfer, printing, and assembly techniques for flexible electronics, in: Advanced Electronic Materials vol. 5, Issue 7, Blackwell Publishing Ltd., 2019, https://doi.org/10.1002/aelm.201800900.
[30] A.G. Demir, B. Previtali, Dross-free submerged laser cutting of AZ31 Mg alloy for biodegradable stents, J. Laser Appl. 28 (3) (2016), https://doi.org/10.2351/1.4944751.
[31] https://refractiveindex.info/?shelf=main&book=Cu&page=Johnson.